Physics of Fluids

Higher order dynamic mode decomposition of an experimental trailing vortex

Cite as: Phys. Fluids **34**, 107116 (2022); https://doi.org/10.1063/5.0117611
Submitted: 01 August 2022 • Accepted: 22 September 2022 • Accepted Manuscript Online: 23 September 2022 • Published Online: 27 October 2022

P. Gutierrez-Castillo, M. Garrido-Martin, T. Bölle, et al.

Physics of Fluids ARTICLE scitation.org/journal/phf

Higher order dynamic mode decomposition of an experimental trailing vortex

Cite as: Phys. Fluids **34**, 107116 (2022); doi: 10.1063/5.0117611
Submitted: 1 August 2022 · Accepted: 22 September 2022 ·
Published Online: 27 October 2022

P. Gutierrez-Castillo,[1,a)] M. Garrido-Martin,[1] T. Bölle,[2] J. H. García-Ortiz,[3] J. Aguilar-Cabello,[1] and C. del Pino[1]

AFFILIATIONS

[1]Universidad de Málaga, Institute for Mechatronics Engineering and Cyber-Physical Systems (IMECH.UMA), Campus de Teatinos, s/n, 29071 Málaga, Spain
[2]Institute of Atmospheric Physics, DLR, Münchener Straße 20, 82234 Weßling, Germany
[3]Departamento de Ingeniería Mecánica y Diseño Industrial, Escuela Superior de Ingeniería, Universidad de Cádiz, Av. Universidad de Cádiz, 10, Puerto Real, 11519 Cádiz, Spain

[a)]Author to whom correspondence should be addressed: paloma_gutierrez@uma.es

ABSTRACT

The decay of trailing vortices is a fundamental problem in fluid mechanics and constitutes the basis of control applications that intend to alleviate the wake hazard. In order to progress, we use the recently developed modal-decomposition technique to identify the governing dynamics in an experimental trailing vortex. A particular emphasis is on the difficulty and usefulness of applying such tools to noisy experimental data. We conducted a water-tunnel experiment at a chord-based Reynolds number $Re = 4 \times 10^4$ using stereoscopic particle image velocimetry measurements over a downstream range of 36 chords. The downstream evolution of the maximum of vorticity suggests that the whole wake can be partitioned into three consecutive regimes. A higher-order dynamic mode decomposition of the streamwise vorticity in each such part of the wake shows that the decay is well approximated by at most three modes. Additionally, our study provides evidence for the existence of several instabilities after the vortex roll up beyond about 6.5 chords.

I. INTRODUCTION

The formation of trailing vortices is due to the finite length of three-dimensional aerodynamic profiles, which appear in applications such as sailing hydrofoils,[1] turbomachinery,[2] or aircraft.[3] Our main interest is in the latter, where there is a pressure difference on both sides of the airfoil that encounters at the end of the wing span at a certain positive angle of attack and, therefore, generates a persistent and highly rotating axial flow in airport runways[4] for a low subsonic, incompressible turbulent regime at high Reynolds numbers $Re \sim 10^6$ (the Reynolds number is defined in Sec. II). In addition, this wake damage occurs even at moderate or low $Re \sim 10^4$ in Unmanned Aerial Vehicles (UAVs).[5,6]

These trailing vortices are in fact the main reason for the restrictive rules in air traffic management[7] and close UAVs flight configuration.[6] The motivation for this work is the possibility to devise an efficient means of vortex alleviation, being a critical concern for safety and economic reasons including, for example, the time reduction between takeoff and landing operations at the airport, the decrease in fuel consumption in aircraft, or the increase in safe control in close UAVs. As a matter of fact, isolated trailing vortices are highly persistent fluid objects that diffuse at an almost viscous rate.[8] A possible strategy to alleviate vortices would be an efficient vorticity reduction using a device that results from the combination of active control[9] and frequency response.[10] For this purpose, it is relevant to have detailed knowledge of the vortex structure to determine a basis for constructing simplified vortex skeletons and low-order flow descriptions.[11] In particular, we focus our attention on the identification of the modes responsible for the vortex decay and their corresponding amplitudes and frequencies. Thus, it is feasible to force these modes with an active control to promote the vortex breakdown.

One alternative for the identification of coherent structures in trailing vortices is the Proper Orthogonal Decomposition (POD).[12,13] This technique processes the modes ordered by relevance in terms of energy. To that end, there is a decomposition of the velocity field with a strong rotational component into a summation containing deterministic spatial functions whose modulation is given by random time

coefficients. In the case of trailing vortices,[14] the most energetic mode has turned out to be $|m| = 1$ and has been associated with low frequencies.

This mode has also been the protagonist in the explanation of the random and erratic motion that appears in the wake, commonly called vortex meandering.[15,16]

Another approach for the characterization of complex experimental flow dynamics present in trailing vortices is the use of Dynamic Mode Decomposition (DMD).[17,18] As reported in a recent review of this method,[19] DMD processes high-dimensional sequential measurements, extracts coherent structures, isolates dynamic behavior, and reduces complex evolution processes to their dominant features and essential components. DMD has recently been improved, introducing the Higher Order Dynamic Mode Decomposition (HODMD).[20,21] This latter method seems to be a useful tool to identify and extrapolate flow patterns[22] and reduced-order models;[23] therefore, it should give a better understanding of the vortex performance and the predominant modes that are responsible for the vorticity decay. As discussed below in Secs. III and IV, HODMD has some disadvantages because it is not straightforward to identify the optimal parameter choices when using raw experimental (noisy) data.[24] However, it is possible to attribute a physical meaning to the most relevant modes when the results have been analyzed carefully. The comparison between DMD/HODMD and POD has been explored, with the former being more appropriate for reconstructing the flow and finding the physical mechanisms underlying the dynamics.[25,26] To the best of our knowledge, there is no implementation of HODMD applied to trailing vortices, which is the novelty of the work.

To sum up, there is considerable need to better understand the dynamics of the wake of both aircraft or UAVs. To take advantage of HODMD, we analyze the modes using two options: (i) the whole experimental spatial domain and (ii) the three different regions into which the wake behavior can be divided, e.g., the near, intermediate, and far fields. Ideally, the HODMD would retain information associated with the vortex decay. This would permit a low-dimensional representation of the decay dynamics of the vortex, which could serve to simplify the vortex mathematical model and reduce the computational burden to its computation.

The paper is organized as follows. First, we introduce the experimental setup as well as the two-component and three-dimensional, 2D3C-PIV data. Second, we describe mathematically, and in a rigorous manner, the algorithm employed. Finally, we show the results using the two alternatives stated above and we draw the main conclusions.

II. OUTLINE OF THE EXPERIMENT

We carried out experimental tests in a towing tank located in the Vehicles Aero-Hydrodynamics Laboratory (Malaga, Spain).[9,27] Figure 1 shows the 3D layout of the experimental arrangement. The support (1) allows different angles of attack between the upstream flow and the wing model, see inset (b). All the results shown correspond to a single angle of attack ($\alpha = 9°$). The scaled wing model used to generate wingtip vortices was a rectangular wing profile with a rounded (half-circular) tip. It has a NACA 0012 wing section which is symmetrical with a maximum thickness of 12 % of the chord. The main dimensions are a semi-span l of 0.2 m and a chord c of 0.1 m, so the aspect ratio AR is equal to 2, see inset (c). This low aspect ratio has been determined by the physical limitations in the experimental setup. However, we find the present aspect ratio $AR = 2$ being sufficiently large to produce a sharp rotating flow behind the wing model, which is the objective of the following dynamic mode decomposition study. The towing tank is 10 m long and 0.5×0.5 m^2 cross section in Perspex® which had a thickness of 25 mm (2) to allow for optical visualizations and three-dimensional Particle Image Velocimetry (2D3C-PIV) measurements of the velocity field. This technique captures velocity information of the whole flow fields in fractions of a second using two consecutive images from the illuminated plane (3). The wing model is vertically assembled on a guide rail (4) that moves (from right to left in the schematic) through the whole towing tank. A chord-based Reynolds number for the flow is given by

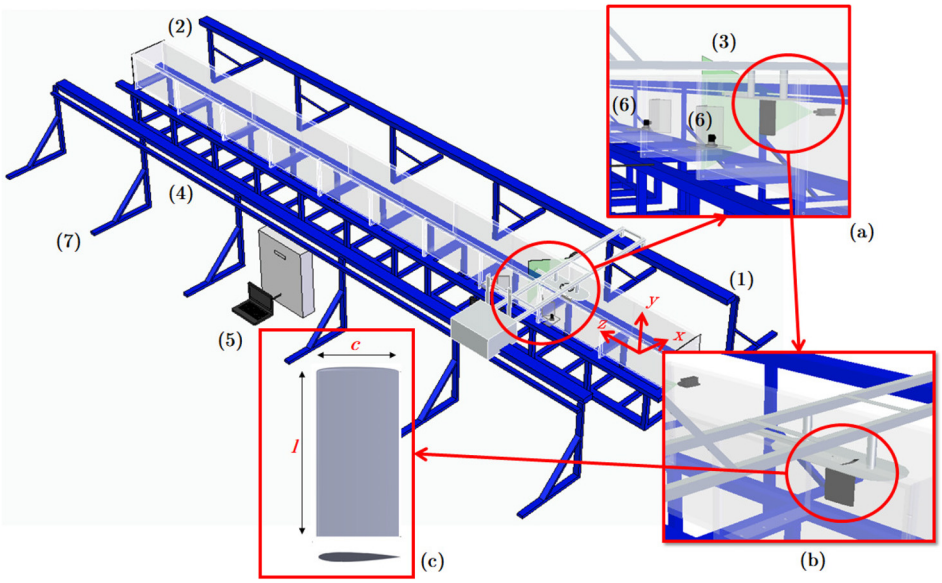

FIG. 1. 3D Schematic of the experimental setup: NACA 0012 wing with *AR* of 2 in a support moving from right to left (1), perspex channel (2), laser sheet (3), guide rail (4), computer to velocity control of guide rail and PIV system (5), high speed cameras (6), and blue iron structure (7). Inset (a) on the right corresponds to zoom in study zone with wing model, cameras, and laser sheet, whereas inset (b) shows a half-span wing model mounted detail with $c = 0.1$ and $l = 0.2$ m, see inset (c).

$$Re = \frac{W_\infty c}{\nu}, \tag{1}$$

where ν is the (temperature dependent) kinematic viscosity of the water and W_∞ is the wing model velocity. The temperature measurement was calculated before running the experiment as the mean value of nine temperature sensors located at different levels along the towing tank. The mean and standard deviation of these measurements were $15.6 \pm 0.2\,^\circ$, so that $\nu = 1.1203\ \mathrm{m^2\,s^{-1}}$. The wing model was pulled at an approximately constant velocity of $W_\infty = 0.448\ \mathrm{ms^{-1}}$ to ensure a chord-based Reynolds number $Re = 4 \times 10^4$. To that end, an electric motor has been installed which provides a velocity between 10^{-2} and 1 $\mathrm{ms^{-1}}$ with an error lower than 0.5 %. The electric motor is controlled by a laptop with feedback by means of an encoder (5), and the control of the acceleration from rest and the final position of the model was set using Matlab® through the USB port. To obtain the images, we seeded the tank with glass silver-coated spheres of 10 μm (HGS-10 from Dantec). These particles are neutrally buoyant in water, thus minimizing their relative motion to the water flow due to gravity and centrifugal forces. The illuminated plane of the flow is located perpendicularly to the wing model movement, and the images are recorded by two high-speed cameras located downstream to the model movement (6). These cameras have their corresponding optical windows to avoid refraction in image capture. The towing tank used two rails made of iron (7). They were mounted with 90° to bear the weight of the water and to guarantee the correct alignment within $\pm 0.1°$.

A 2D schematic layout is shown in Fig. 2 to aid readers in understanding the key 2D-3C PIV layout. The displacement of the wing model from left to right, indicated by a blue arrow, is shown along with the Cartesian reference frame. Thus, the schematic shows precisely when the wing model passed through the laser sheet and the first velocity field was measured ($z/c = 0$). On the other hand, by placing water-filled prisms in the air–glass–water interface, the refraction of the interface has been corrected. Two transparent

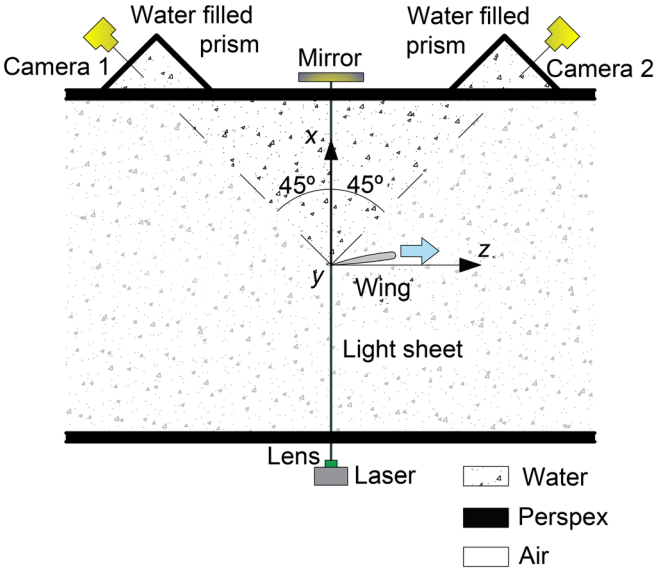

FIG. 2. 2D Schematic of the experimental setup.

Plexiglas prismatic windows were attached to the lateral sides of the channel working section. These windows, which faced normally the cameras by forming an angle of 45° with the Plexiglas walls of the channel, were filled with water and adjusted through watertight unions to the channel walls.

As the experiments are conducted in a towing water tank, the distance and sampling time over which the airfoil can maintain a constant speed are 1 or 1 m/$W_\infty = 2.5$ s, respectively. Hence, the wing model goes from rest to the desired speed in the first meter with a linear ramp by using the dc motor and its speed control. Afterward, the wing model has a constant velocity; therefore, the laser sheet is placed at 3 m from the beginning of the towing tank. Figure 1 shows the wing model at the point where the wing model has almost reached the constant velocity, but the laser sheet has not yet been reached.

As described in Sec. I, vortices are so sensitive that they are disturbed by turbulence, which causes random shifts in the center of the vortex. This phenomenon is known as meandering, and it hinders experimental measurements. There are well-established methods in the literature to correct for wandering techniques.[16,28–30] In our case, this phenomenon of erratic movement of the vortex core is not very pronounced due to the low turbulence in the towing tank.

A 2D3C-PIV system was used to measure the velocity field of the wingtip vortex. Consequently, a three-dimensional description of the vortex is compiled in the control plane. As mentioned above, this plane is perpendicular to the movement of the airfoil, and it has a fixed location, whereas the wing model moves through the towing tank. Subsequently, we examine the velocity field in each plane (x, y) alongside the axial coordinate (z). The 2D3C-PIV system consists of three components: (i) a laser sheet (3) that is less than 1 mm thick in the measurement section obtained using three 0.5 W green laser sources (532 nm-model SDL-532–500T) in conjunction with a set of lenses (cylindrical lens of −6.25 mm focal length), and a mirror that was installed in front of the laser plane to obtain a better illumination sheet, (ii) two high-speed monochrome cameras together with mechanical connecting fittings to implement the Scheimpflug system (6) model PixeLINK PL-D732MU-T which records images of 2.2 Mpx up to 170 fps, and a 25 mm RICOH lens (model FL-CC2514–2M) and f/2.8, (iii) synchronizer and the use of software PixeLINK Capture OEM, and finally, (iv) a photoelectric cell to synchronize the experimental setup. Only a maximum frame rate of 120 fps was required for this experimental work, although lower frame rates were also used; hence, the authors need to warn that the images required to do 2D3C-PIV could have been obtained with a standard camera with slow motion application. This experimental setup allowed us to obtain the wing wake evolution over a distance of about 36c from the onset of motion. We set the exposure time to 8 ms with the global electronic shutter. The calibration of a 2D3C-PIV imaging setup relies on images of a planar calibration target placed alongside the light sheet plane. This calibration target consisted of an equally spaced grid of dot markers (10 mm) that were easily detected with simple image processing techniques. The PIV algorithm employed was DPIVSoft which performs a double pass PIV method with window deformation of 32 × 32 pixels, being the time step between images the inverse of the frame rate. Data reduction algorithms provided the true particle displacement and 3D velocity vector field at the illuminated plane.[31]

III. HIGHER ORDER DYNAMIC MODE DECOMPOSITION

A. A brief description of the basis

We employ the Higher Order Dynamic Mode Decomposition (HODMD) proposed by Le Clainche and Vega.[20] A similar theory has been developed by Kamb *et al.*[32]

Experiments provide us with a sample of the continuous Eulerian flow fields on a discrete measurement grid of dimension $M \times N$, where $M = M_x M_y$ and N are the number of spatial and temporal measurement points, respectively. Concatenating the spatial data at each time instance into a vector, we obtain an ordered sequence of length N where each element is a $\mathbb{R}^M$-dimensional vector called snapshot. It is convenient to assemble the data into a $\mathbb{R}^{M\times N}$-dimensional snapshot matrix $\boldsymbol{W}_1^N = [\boldsymbol{w}_1, \boldsymbol{w}_2, \ldots, \boldsymbol{w}_N]$, with $\boldsymbol{w}_n := \boldsymbol{w}(t_n)$ and $t_n = (n-1)\Delta t$ for $n = 1, 2, \ldots, N$. In our case, we consider the data of the streamwise vorticity ζ since the vorticity decomposition has captured the fluctuating enstrophy more efficiently than the equivalent velocity field decomposition for a given number of POD modes in the backward-facing step problem.[11] However, we will continue with the generic definition of the vector $\boldsymbol{w}$ in this section for mathematical description purposes.

It is a fundamental aspect of DMD that the temporal order of the data are taken into account, unlike, for instance, in Snapshot Proper Orthogonal Decomposition (POD) where the temporal ordering of the snapshots is irrelevant for the POD modes (spatial patterns) and associated eigenvalues. This is consistent with the assumption of a stationary random process underlying POD.[33] On the other hand, DMD makes the fundamental assumption that the time sequence of snapshots follows from a linear dynamics. That is,

$$\boldsymbol{w}_{n+d} = \sum_{i=1}^{d} \boldsymbol{A}_i \boldsymbol{w}_{n+i-1} \quad \text{with} \quad n = 1, 2, \ldots, N-d \quad \text{and} \quad d \geq 1, \tag{2}$$

where $\boldsymbol{A}_i \in \mathbb{R}^{M\times M}$ is the propagator of the linear dynamics. A linear approach even for nonlinear dynamics has been justified by interpreting (2) in terms of Koopman mechanics.[17] In this framework, we maintain that the dynamics is governed by some nonlinear dynamical system which, however, is not directly observable. What we actually measure are but functions mapping the states of the system onto a measurable observable, of which the snapshots are approximations. For this reason, (2) is called (higher order) Koopman assumption. For $d = 1$, (2) involves only a mapping between two subsequent time steps, which is the assumption of (classical) DMD.[17,18]

However, we can formally reduce the general problem (2) to a one-step evolution upon working in a d-dimensional embedding space. Working in high-dimensional spaces is a commonly employed strategy to unfold the apparent complexity of observed dynamics. One state in the embedding space is defined as the sub-ensemble of time-lagged snapshots, viz. $\tilde{\boldsymbol{w}}_n := (\boldsymbol{w}_n, \boldsymbol{w}_{n+1}, \ldots, \boldsymbol{w}_{n+d-1}) \in \mathbb{R}^{dM}$. The propagator in the embedding space accordingly becomes a $\mathbb{R}^{dM\times dM}$-dimensional matrix of the transpose companion type. That is, $\tilde{A}_{ij}$ is of (upper-diagonal) shift type for $i = 1, 2, \ldots, (d-1)M$ and $j = 1, 2, \ldots, dM$, while the entries in the lowest row (i.e., for $i = (d-1)M + 1, \ldots, dM$) are the propagators in (2). With this, we get the one-step problem

$$\tilde{\boldsymbol{w}}_{n+1} = \tilde{\boldsymbol{A}}\tilde{\boldsymbol{w}}_n, \quad n = 1, 2, \ldots, N-d, \tag{3}$$

in the d-dimensional embedding space.

The purpose of the DMD is a characterization of the propagator (in this context called Koopman or composition operator[17]) in terms of its point spectrum.[34] The associated eigenvalue problem for $\tilde{\boldsymbol{A}}$ has a maximum of dM eigenvalues $\lambda_j \in \mathbb{C}$ and associated eigenvectors $\boldsymbol{q}_j \in \mathbb{C}^{dM}$ (complex conjugation, degeneracy, etc. depend on the data). The adjoint of the Koopman operator is the Perron–Frobenius operator and has eigenvalues and eigenvectors $\bar{\lambda}_j$ and $\boldsymbol{p}_j$, respectively (an overbar denotes complex conjugation). The direct and adjoint eigenvectors are biorthogonal $(\boldsymbol{p}_i, \boldsymbol{q}_j) = \delta_{ij}$ with respect to the inner product $(\cdot, \cdot)$ on $\mathbb{R}^{dM}$. An expansion of $\tilde{\boldsymbol{w}}_{n+1}$ in the eigenvectors thus reads

$$\tilde{\boldsymbol{w}}_{n+1} = \sum_j a_j(t_{n+1})\boldsymbol{q}_j \quad \text{where} \quad a_j(t_{n+1}) = (\boldsymbol{p}_j, \tilde{\boldsymbol{w}}_{n+1}). \tag{4}$$

It follows at once from (3) that $\tilde{\boldsymbol{w}}_{n+1} = \tilde{\boldsymbol{A}}^n \tilde{\boldsymbol{w}}_1$ by recurrence. By virtue of the linearity of $\tilde{\boldsymbol{A}}$, hence,

$$\tilde{\boldsymbol{w}}_{n+1} = \tilde{\boldsymbol{A}}^n \tilde{\boldsymbol{w}}_1 = \sum_j a_j(0)\tilde{\boldsymbol{A}}^n \boldsymbol{q}_j = \sum_j a_j(0)\lambda_j^n \boldsymbol{q}_j. \tag{5}$$

Let $\lambda_j \neq 0$, then we can define the transformation

$$\lambda_j := e^{s_j \Delta t} \quad \Longleftrightarrow \quad s_j := \delta_j + \mathrm{i}\omega_j = \Delta t^{-1} \ln \lambda_j. \tag{6}$$

We order the amplitudes in decreasing order $a_1 \geq a_2 \geq \cdots > 0$. Let $\epsilon_{DMD} \geq 0$, we keep only the $R \leq dM$ largest amplitudes such that

$$\frac{a_{R+1}}{a_1} \leq \epsilon_{DMD} \tag{7}$$

holds for the leading relative error. We call R the ϵ_{DMD} spectral complexity. The approximate reconstruction of the measured data

$$\tilde{\boldsymbol{w}}_n \approx \tilde{\boldsymbol{w}}_n^{(R)} := \sum_{r=1}^{R} a_r \boldsymbol{q}_r e^{(\delta_r + \mathrm{i}\omega_r)(n-1)\Delta t}, \quad n = 1, 2, \ldots, N-d. \tag{8}$$

For given R of the reconstruction (8), the DMD modes $\boldsymbol{q}_r$ span a manifold of dimension $S := \dim\mathrm{span}\{\boldsymbol{q}_1, \boldsymbol{q}_2, \ldots, \boldsymbol{q}_R\} \leq \min\{dM, R\}$, which we call ϵ_{spec}-spatial complexity.

B. The algorithm

A detailed description of the algorithm of classical DMD can be found in several research papers.[18,35] A comparison and extension to HODMD is given in Le Clainche and Vega.[20] We would like to mention here the essential aspects of the procedure which are important for the present study.

We refer to DMD and HODMD as DMD-d in an encompassing manner.[20]

1. Step 1: Dimension reduction

The first step of the DMD-d algorithm is a coordinate transformation together with a truncation of the representation. The result is a filtering and dimension reduction.

SVD of the snapshot matrix $\boldsymbol{W}_1^N = \boldsymbol{U}\boldsymbol{\Sigma}\boldsymbol{V}^*$.

(a) Let $J_r \leq \min\{M, N\}$ be the rank of the snapshot matrix, we define the relative truncation error (ratio of Frobenius norms)

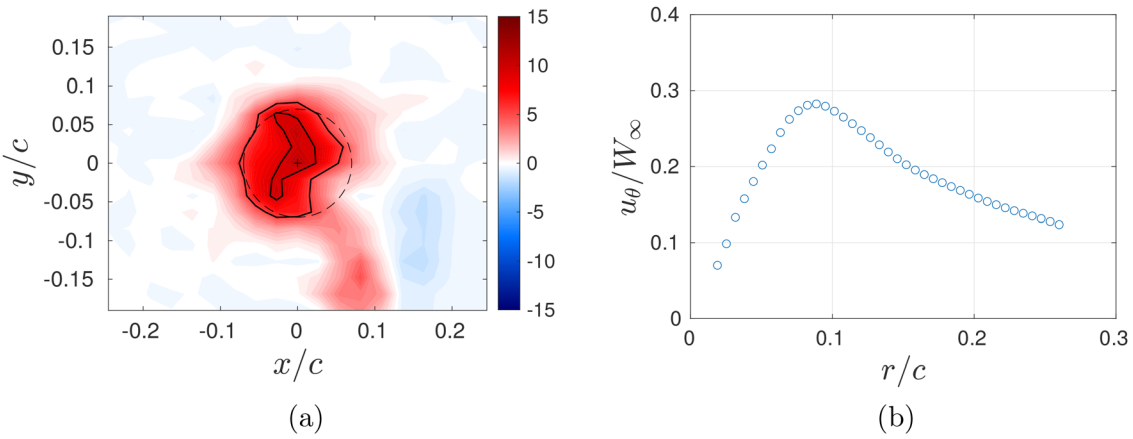

FIG. 3. Vortex flow at $z/c = 0$: (a) non-dimensional vorticity and (b) radial profile of the azimuthal velocity.

$$\mathcal{E}(J_\epsilon) := \sqrt{\frac{\sum_{j=J_\epsilon+1}^{J_r} \sigma_j^2}{\sum_{j=1}^{J_r} \sigma_j^2}} \leq \epsilon_{\text{SVD}}, \tag{9}$$

associated with a representation in the leading $J_\epsilon \leq J_r$ singular modes for some predefined threshold $\epsilon_{\text{SVD}} \geq 0$. We refer to the truncated SVD matrices as $\bar{\boldsymbol{U}} \in \mathbb{R}^{M\times J_\epsilon}$, $\bar{\boldsymbol{\Sigma}} \in \mathbb{R}^{J_\epsilon\times J_\epsilon}$, and $\bar{\boldsymbol{V}}^* \in \mathbb{R}^{J_\epsilon\times N}$. (An overbar denotes truncation.)

(b) We define the reduced snapshot matrix with respect to the truncated basis

$$\hat{\boldsymbol{W}}_1^N := \bar{\boldsymbol{U}}^* \bar{\boldsymbol{W}}_1^N = \bar{\boldsymbol{\Sigma}} \bar{\boldsymbol{V}}^* \in \mathbb{R}^{J_\epsilon\times N}, \tag{10}$$

as the projection of the full snapshot matrix $\boldsymbol{W}_1^N$ onto the leading J_ϵ singular modes. (A hat denotes reduction due to projection, possibly with respect to a truncated singular-vector set.) SVD is a coordinate transformation to the principal components, spanning an ellipse with respective axes' lengths equal to the singular values. From this picture, we see that (9) and (10) imply that we are working in the leading principal components with a relative error of ϵ_{SVD}. Put differently, we work only with the time series of expansion coefficients in the singular-vector expansion. We pass back to the full (yet, truncated) space by multiplying with $\bar{\boldsymbol{U}} \in \mathbb{R}^{M\times J_\epsilon}$.

The snapshot matrix in the embedding space reads

$$\tilde{\boldsymbol{W}}_1^{N-d+1} = [\tilde{\boldsymbol{w}}_1, \tilde{\boldsymbol{w}}_2, \ldots, \tilde{\boldsymbol{w}}_{N-d+1}] \in \mathbb{R}^{dM\times(N-d+1)}, \tag{11}$$

and in the reduced coordinates

$$\hat{\tilde{\boldsymbol{W}}}_1^{N-d+1} = [\hat{\tilde{\boldsymbol{w}}}_1, \hat{\tilde{\boldsymbol{w}}}_2, \ldots, \hat{\tilde{\boldsymbol{w}}}_{N-d+1}] \in \mathbb{R}^{dJ_\epsilon\times(N-d+1)}, \tag{12}$$

respectively. This snapshot matrix in the time-lagged reduced and truncated coordinates is again reduced and truncated along the same lines described above. This yields $\hat{\hat{\boldsymbol{W}}}_1^{N-d+1} \in \mathbb{R}^{J'_\epsilon\times(N-d+1)}$, where $J'_\epsilon \leq \operatorname{rank} \hat{\tilde{\boldsymbol{W}}}_1^{N-d+1}$.

2. Step 2: Reduced Koopman operator

In the second step, we compute the reduced Koopman operator from a purely data-driven approach.

(a) We can express the Koopman assumption (2) in the reduced coordinates. Therefore, note that the nth snapshot in the truncated representation is $\bar{\boldsymbol{w}}_n = \bar{\boldsymbol{U}}\bar{\boldsymbol{\Sigma}}\bar{\boldsymbol{v}}_n$, where $\bar{\boldsymbol{v}}_n$ is the nth column of $\bar{\boldsymbol{V}}^*$, and $\hat{\boldsymbol{w}}_n = \bar{\boldsymbol{\Sigma}}\bar{\boldsymbol{v}}_n$ the nth reduced snapshot. Projecting (2) onto the reduced singular-vector space and using linearity readily yields

$$\hat{\boldsymbol{w}}_{n+d} = \sum_{i=1}^{d} \hat{\boldsymbol{A}}_i \hat{\boldsymbol{w}}_{n+i-1},$$

upon defining the reduced Koopman operator as the projection $\hat{\boldsymbol{A}}_i := \bar{\boldsymbol{U}}^* \boldsymbol{A}_i \bar{\boldsymbol{U}}$. Apparently, the Koopman assumption in the truncated and reduced coordinates is structurally identical to (2), thus going to the embedding space, we get a one-step problem structurally identical to (3), only replacing the entries by the respective reduced forms. This implies $\hat{\tilde{\boldsymbol{A}}} \in \mathbb{R}^{dJ_\epsilon\times dJ_\epsilon}$ for the reduced Koopman operator in the embedding space.

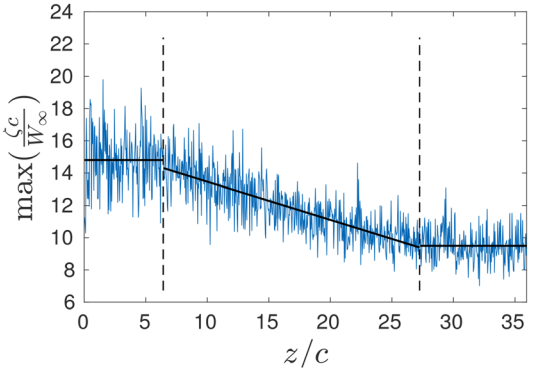

FIG. 4. Downstream evolution of the vorticity maximum. Dashed lines indicate the partition into the three different wake regimes identified by linear regression (solid black lines).

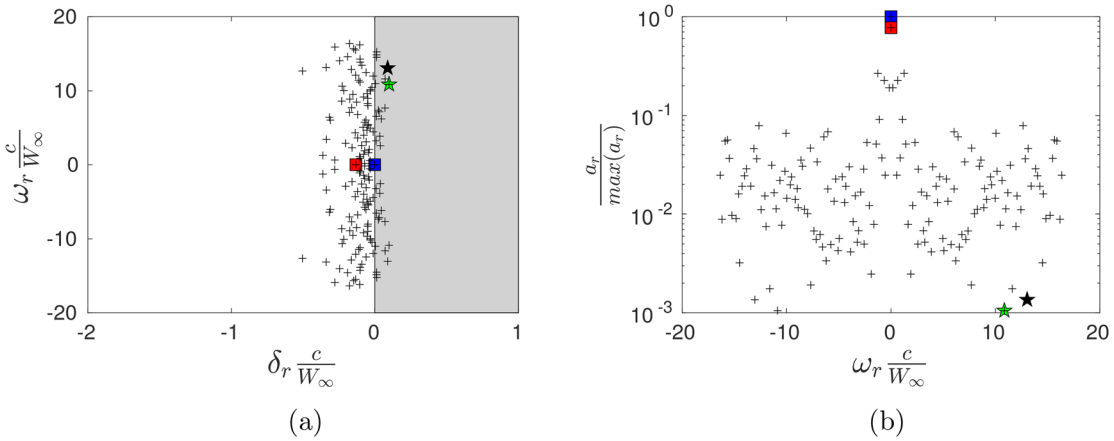

FIG. 5. HODMD analysis of the whole field: (a) amplification factor vs frequency and (b) frequencies vs amplitude. In both pictures, the modes with highest amplitude are marked with squares: mode 1 in blue and mode 2 in red. The most unstable modes are marked with colored stars: mode 1 in green and mode 2 in black.

(b) Since $\boldsymbol{A}_i$ are not known explicitly, we cannot compute the projection $\hat{\boldsymbol{A}}_i$ directly. Instead, we compute it by means of the pseudoinverse. For this purpose, we write the one-step, higher-order Koopman assumption in the reduced coordinates $\hat{\tilde{\boldsymbol{W}}}_2^{N-d+1} = \hat{\tilde{\boldsymbol{A}}}\hat{\tilde{\boldsymbol{W}}}_1^{N-d} = \hat{\tilde{\boldsymbol{A}}}\hat{\tilde{\boldsymbol{U}}}\hat{\tilde{\boldsymbol{\Sigma}}}\hat{\tilde{\boldsymbol{V}}}^*$, which yields $\hat{\tilde{\boldsymbol{A}}} = \hat{\tilde{\boldsymbol{W}}}_2^{N-d+1}\hat{\tilde{\boldsymbol{V}}}\hat{\tilde{\boldsymbol{\Sigma}}}^{-1}\hat{\tilde{\boldsymbol{U}}}^*$.

We then solve the eigenvalue problem $\hat{\tilde{\boldsymbol{A}}}\hat{\tilde{\boldsymbol{q}}}_r = \lambda_r\hat{\tilde{\boldsymbol{q}}}_r$ and use the first J_ϵ components of the eigenvector in the reconstruction of the data

$$\hat{\boldsymbol{w}}_n \approx \hat{\boldsymbol{w}}_n^{(R)} := \sum_{r=1}^{R} a_r\hat{\boldsymbol{q}}_r e^{(\delta_r+\mathrm{i}\omega_r)(n-1)\Delta t}, \quad n = 1, 2, \ldots, N. \tag{13}$$

For the sake of discussing the experimental results, it is convenient to associate time and space increments according to $\Delta z = W_\infty \Delta t$, whereas W_∞ denotes the pulling velocity. This yields the downstream (*D*ynamic) evolution of the *r*th mode as follows:

$$D_r(t) = \exp\left((\delta_r + \mathrm{i}\omega_r)t\right) = \exp\left[\left(\frac{\delta_r c}{W_\infty} + \mathrm{i}\frac{\omega_r c}{W_\infty}\right)\frac{z}{c}\right]. \tag{14}$$

Data are continuously collected for about 8 s between the starting and the end points. Despite this, due to the small changes in the wing tip vortex that occur as it evolves temporally without the presence of external turbulence, this time between the first and last snapshot does not significantly alter the flow patterns as well as the development of eventual instabilities within the vortex. With this experimental setup, we are also able to have many sampling points staggered in time to perform an accurate calculation through HODMD. A similar experimental setup for wing-tip vortices was presented in Ghimire and Bailey.[36]

IV. RESULTS

A. Overview of the vortex flow

Trailing vortices observed in experiments are associated with a broadband spectral signature spanning all resolved scales. We use HODMD to identify the governing dynamics associated with vortex decay and instability.

We base our HODMD analysis on the streamwise vorticity field ζ in equidistant measurement planes perpendicular to the wing motion. We sampled data over the downstream range $z/c \in [0, 36]$ with a total of $N = 963$ planes, spaced at a constant distance of $3.73 \times 10^{-2}c$, as detailed in Sec. II. Streamwise vorticity $\zeta = \partial u/\partial y - \partial v/\partial x$ was computed with a second-order, central finite difference scheme from the velocity data directly obtained in the PIV measurements non-dimensionalized using the pulling velocity W_∞ and chord c as characteristic velocity and length, respectively.

Since we are interested in the vortex dynamics, we restrict the analysis to an observation window centered around the instantaneous vortex center in each measurement plane. The vortex center is defined as the location of the maximum of the vorticity field,[37] and the observation window was chosen to extend over nine grid points to each side of the center. Therefore, the computational domain extends over approximately three core radii r_1, see its definition in (16).

Experimental results allow us to clearly identify the vortex shape when representing vorticity. Figure 3(a) shows the dimensionless vorticity $\zeta c/W_\infty$ in the first measurement plane at $z/c = 0$ where the vortex structure is clear. Black solid lines are representing 50% and 85% of the maximum of vorticity. A cross marker and a dashed black circle of radius $r_1 = 0.07c$ have been added to illustrate the vortex center and the vortex core, respectively. Along the negative y coordinate, we still see a trace of the roll up of the trailing vorticity sheet. At the same time, the main vortex already approaches an approximately axisymmetric shape.

Figure 3(b) depicts the radial profile of the associated non-dimensional azimuthal velocity in the same measurement plane at

TABLE I. Comparison of the results obtained from the various domains considered.

Domain	Snapshots	Modes	Physical modes	Unique physical modes
Whole	963	792	158	80
Near	172	63	11	6
Intermediate	558	420	87	45
Far	233	122	23	12

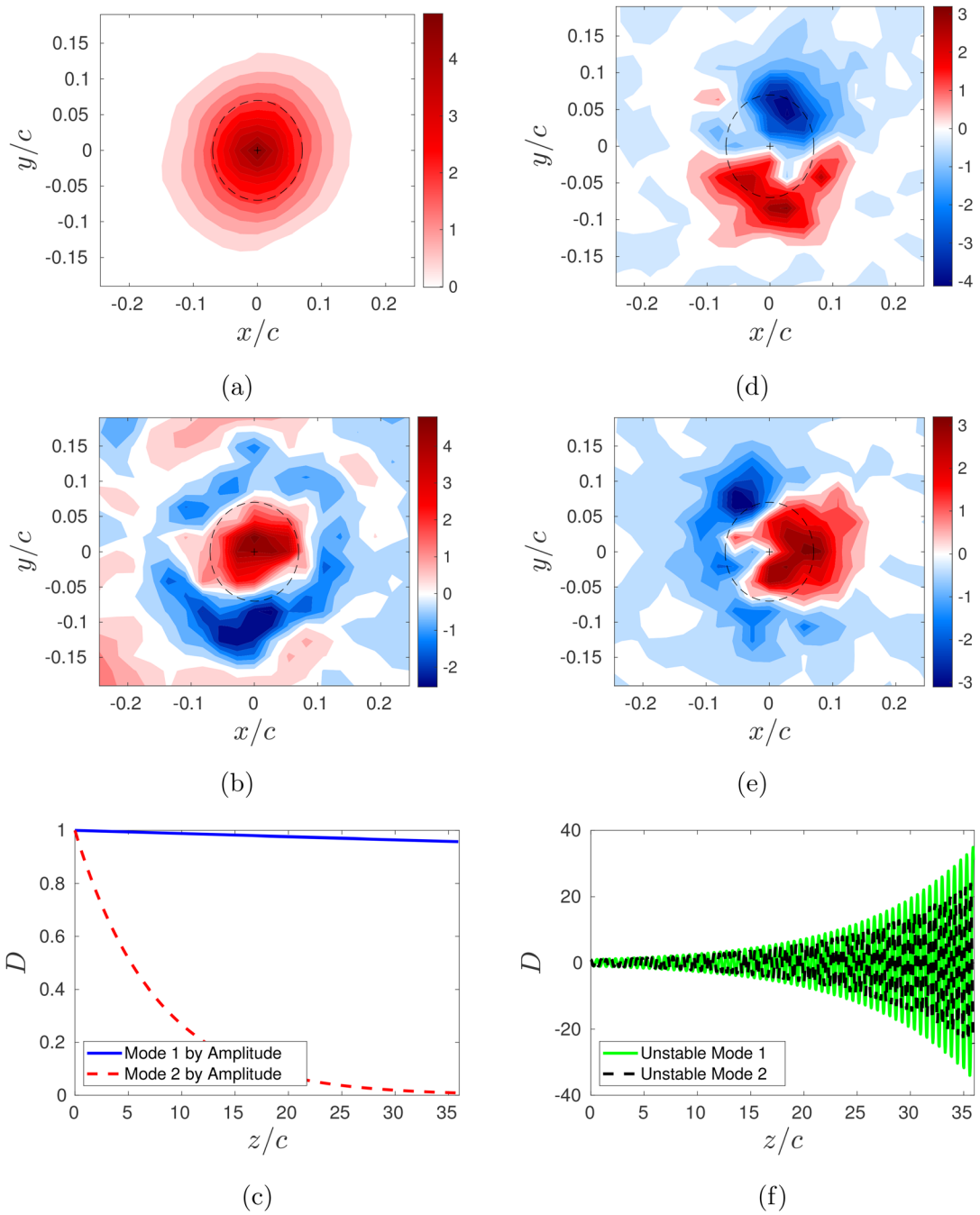

FIG. 6. HODMD analysis over the whole field: (a) and (b) real part of the leading HODMD modes $\boldsymbol{q}$ in terms of amplitude, (c) the associated temporal dynamics, (d) and (e) real part of the leading HODMD modes $\boldsymbol{q}$ in terms of decreasing amplification factor δ_n, and (f) the associated dynamics.

$z/c = 0$, obtained by taking the azimuthal average in the measurement plane, i.e.,

$$u_\theta(r, z = \text{const}) := \frac{1}{2\pi}\int_0^{2\pi} u_\theta(r, \theta, z = \text{const})\mathrm{d}\theta. \tag{15}$$

The integral in (15) is approximated by a sum over 30 points in the azimuthal coordinate (i.e., 12%). It is observed that the radial profile of the azimuthal velocity increases almost linearly up to a peak and thereafter its value drops monotonically. The radial coordinate at the maximum of azimuthal velocity

$$r_1(z) := \arg\max_r u_\theta(r, z), \tag{16}$$

is called core radius. From Fig. 3(b), we infer $r_1(0)/c \approx 9 \times 10^{-2}$. This value increases smoothly up to $r_1(36c)/c \approx 11 \times 10^{-2}$ at the end of the experimental domain. On the other hand, the peak starts at $v_\theta(0)/W_\infty \approx 0.28$ and it decreases till $v_\theta(36c)/W_\infty \approx 0.22$.

Figure 4 shows the downstream evolution of the maximum of dimensionless vorticity over the measurement range. The trend of the vorticity maximum shows a clear distinction, suggesting to separate the wake into three different z regimes, which we refer to as near, intermediate, and far fields for convenience. This separation is indicated by adding vertical dashed lines to Fig. 4. This partition of the whole wake into three regimes is based on the best linear fit in the whole domain, requiring the approximation of the near and far field to be a horizontal line (the linear approximations are shown as solid black lines in Fig. 4). That is, the division of the wake is at the streamwise coordinates that minimize R^2, where R is the linear regression parameter. According to this definition, the near field ranges approximately within $z/c \in (0, 6.42)$, the intermediate field is identified with the range $z/c \in (6.42, 27.25)$, and the far field stretches beyond this point to the end of the measurement domain. As will be explained below, this separation in three areas has a double advantage: on the one hand, a better reconstruction of the vortex and its decay and, on the other hand, the knowledge of the area where unstable modes first appear. Note also that in the near field the vortex core radius as well as the peak of azimuthal velocity are oscillatory, having a mean and standard deviation of $r_1/c \approx 7 \times 10^{-2} \pm 8 \times 10^{-3}$ and max $u_\theta(r, z) \approx 0.3 \pm 0.01$, respectively, for $z/c \in (0, 6.42)$.

B. Higher-order DMD

We selected the values of d, ε_{SVD}, and ε_{DMD} according to the particular flow physics and purpose of analysis.[20] In particular, we chose $\varepsilon_{SVD} = 0.025$ to filter the error coming from the experimental data, as explained in Sec. III. The number of DMD modes that attained for the expansion is, however, determined by $\varepsilon_{DMD} = 10^{-3}$, see Sec. III. Finally, we made a choice of $d = 110$ to minimize the RMS error. This value of d is consistent with previous studies, indicating that a good estimation of d is about 10% of the total number of snapshots.[21]

1. Results using the whole z domain

We have first applied the HODMD on the whole domain with a totality of $N = 963$ snapshots, yielding 792 modes for the selected pair of parameters, ε_{SVD}, and ε_{DMD}. It is useful to mention that not all of the modes contribute equally to the vortex dynamics. To find the physically relevant modes, let us first recall that the downstream evolution of the rth mode is governed by Eq. (14), which is parametrized by the amplification factor δ_r and the angular frequency ω_r. As a necessary condition for a mode to be physically pertinent, we require that it lies at the intersection of the parameter space with a sufficiently small decay and frequency. Thus, we avoid very short-lived transients or high-frequency modes associated with noise in the experiment.

To retain only weakly damped modes, we restrict to amplification factors for which $\delta_r \frac{c}{W_\infty} > -2$. This threshold corresponds to the discarding of modes that attenuate to less than 5% of their initial amplitude within about $z/c = 1.5$. Note that this threshold only removes a few modes, two in the case of the whole domain.

To guarantee sufficient sampling of the temporal evolution, we neglect modes with very high frequency that are likely to be associated with experimental noise or that are not resolved properly taking into account our frame rate in the experiment. In fact, the vortex dynamics are not expected to have so high frequencies.[14,16] This step allows reducing significantly the number of modes. Specifically, we have chosen signals with are sampled with at least ten points, equivalent to $|\omega_r \frac{c}{W_\infty}| > 16.79$.

The restrictions described above reduce the overall 792 modes to a maximum of 158 modes that are potentially physically meaningful. Figure 5 shows the amplitudes, frequencies, and damping factors associated with these modes. The leading modes in order of amplitude a_r and amplification factor δ_r are marked with squares and stars, respectively. Since our data are real-valued, the HODMD modes must come in complex-conjugate pairs or be real.

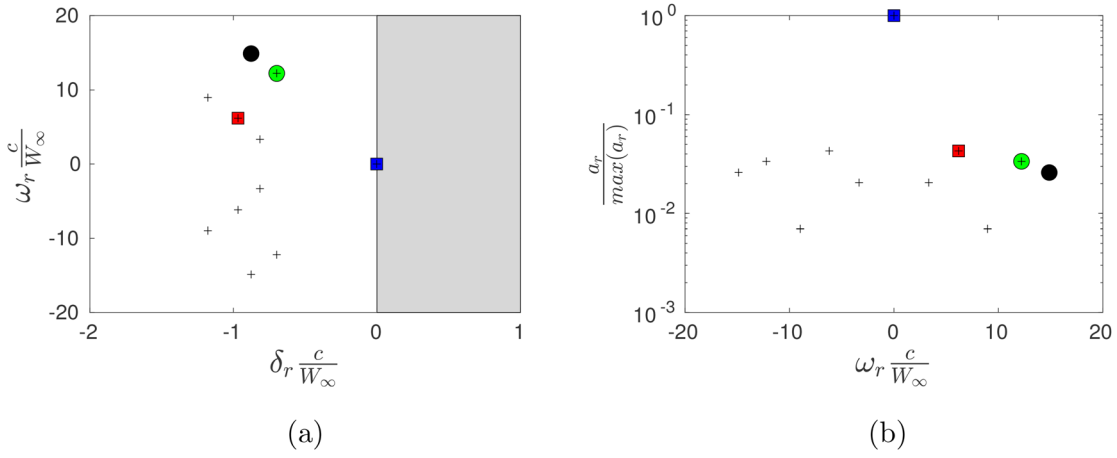

FIG. 7. HODMD analysis to the near field: (a) amplification factor vs frequency and (b) frequencies vs amplitude. In both pictures, the modes with highest amplitude are marked with squares: mode 1 in blue and mode 2 in red. The modes with highest non-zero δ are marked with colored circles: mode 1 in green and mode 2 in black.

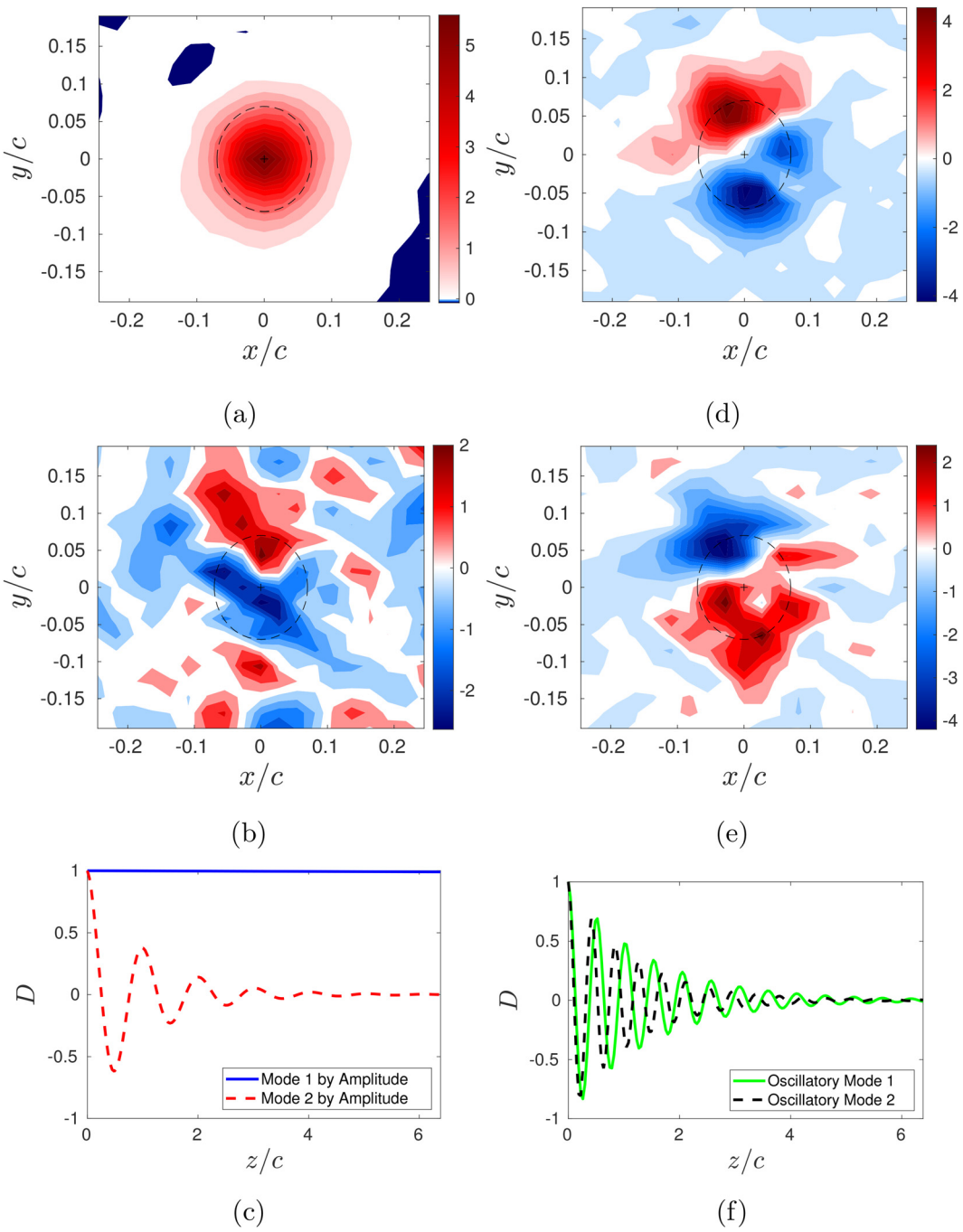

FIG. 8. Analysis over the near field: (a) and (b) real part of the leading HODMD modes $\boldsymbol{q}$ in terms of amplitude, (c) the associated temporal dynamics, (d) and (e) real part of the leading HODMD modes $\boldsymbol{q}$ in terms of decreasing amplification factor δ_r, and (f) the associated dynamics.

There are two types of HODMD modes: (i) those associated with real values and (ii) others corresponding to complex-conjugate pairs. In the case of computing the HODMD on the whole field, there are two modes associated with real values and the rest are complex-conjugate pairs. Each one of the conjugate modes has the same spatial structure and damping frequency, so we consider only 80 unique modes. Table I shows in the first row a summary of the number of modes considered for the whole domain taking into account the

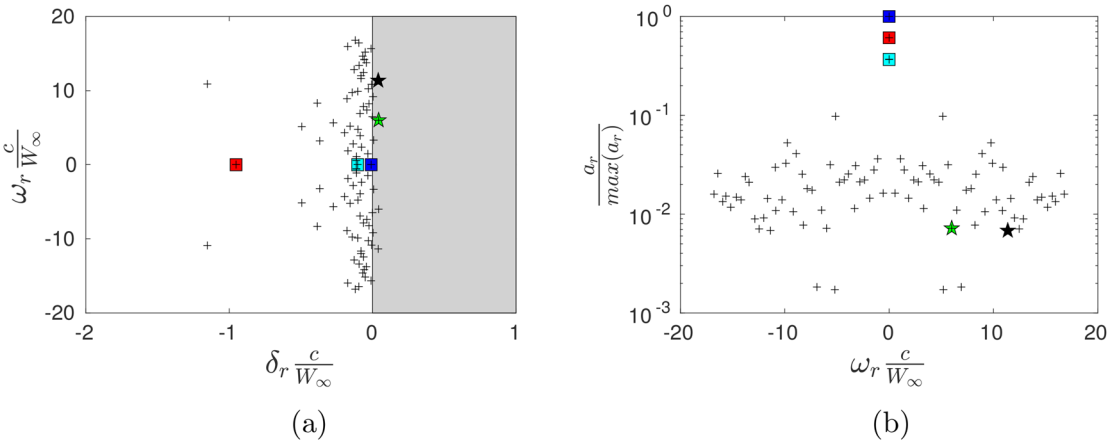

FIG. 9. HODMD analysis of the intermediate field: (a) amplification factor vs frequency and (b) frequencies vs amplitude. In both pictures, the modes with highest amplitude are marked with squares: mode 1 in blue, mode 2 in red, and mode 3 in cyan. The most unstable modes are marked with colored stars: mode 1 in green and mode 2 in black.

different criteria mentioned above. The remaining rows in Table I summarize the HODMD results for each of the three regions, i.e., near, intermediate, and far.

Figures 6(a) and 6(b) show the spatial structure of the two modes of highest amplitude a_r together with their downstream evolution in (c). Both of them are cases of purely real (i.e., non-oscillating) modes, and they exhibit nearly axisymmetric vorticity patterns, $m = 0$. This relationship between axisymmetric modes and real modes is found throughout this investigation. For the analysis of the whole domain, we find that modes 1 and 2, although having similar amplitudes a_r, are associated with strongly different decay rates $|\delta_1| \ll |\delta_2|$. Therefore, the downstream evolution of both modes is significantly different. The combination of these two modes captures the tendency of the vortex decay depicted in Fig. 4.

While the leading non-oscillating modes represent the evolution of the mean, the oscillatory contributions (so-called as they are associated with $\omega \neq 0$) represent fluctuations. Oscillatory modes correspond to multi-polar spatial patterns. In particular, the unstable modes have dipolar pattern in the vorticity. Figures 6(c) and 6(d) depict the two most unstable modes together with the dynamic evolution in (e). HODMD yields a totality of 15 unstable modes for the whole domain and all of them are associated with a dipole pattern (Tables II–V).

Finally, it is important to remark than the spatial representation of the different modes give the same order of magnitude, see Figs. 6(a), 6(b), 6(d), or 6(e). Therefore, it is feasible to obtain an estimation of the relevance of the mode contribution from the analysis of both the amplitude a_r and the parameter δ_r, see Eq. (13). This characteristic is valid for any spatial domain to which HODMD is applied in this investigation.

2. Results dividing the z domain in three regions

As mentioned above, the fluid flow shows different structures for different areas along the z domain. Therefore, we have divided our z domain into three different regions and computed HODMD in the near, intermediate, and far fields. We retain the same HODMD parameters, that is, $\varepsilon_{SVD} = 0.025$, $\varepsilon_{DMD} = 10^{-3}$, and $d = 110$ to allow a comparison with those previous computations shown for the whole domain.

a. Near field. This spatial domain relates to the wake region where $z/c \in (0, 6.42)$. We obtain 63 modes from HODMD. After applying the restrictions on δ_r and ω_r to compute the physical relevant modes, we obtain a set of 11 modes, 6 of them being unique. The amplitude, frequency, and decay associated with these modes are shown in Fig. 7. Note that there is only a real mode in this region, having an amplitude at least an order of magnitude greater than the complex modes. The two modes with greater amplitude a_r are marked with squares in Fig. 7, whereas the two with maximum non-zero δ_r are depicted in circles. Since all non-zero δ_r are negative in this near field, we can conclude that there is no unstable mode in this region. However, these latter two modes with the greatest non-zero δ_r will follow a dynamic evolution with the slowest decay, and therefore, they are more relevant to the structures along this z domain.

The leading two HODMD modes in order of decreasing amplitude a_r are presented in Figs. 8(a) and 8(b) with their associated dynamics shown in Fig. 8(c). Mode 1 is associated with the mean flow and exhibits nearly constant D, as expected from the behavior shown by the maximum vorticity. The second mode in order of amplitude is a oscillatory becoming very weak at about half of the z domain in the near region. This is also the case for the two modes in order of decreasing non-zero δ_r, see Fig. 8(f), both of them having a dipole-like spatial structure, as shown in Figs. 8(d) and 8(e).

b. Intermediate field. The intermediate field corresponds to the z domain ranging between $6.24c$ and $27.25c$. This region is associated with the most obvious vortex decay, see Fig. 4. Therefore, its understanding is deemed crucial for any application targeting vortex alleviation. The results provided by HODMD in this region are more intricate than in the near field having 45 unique physically relevant modes. The amplitude, frequency, and decay associated with these modes are shown in Fig. 9. It is observed that there are three real modes which are also the modes with the highest amplitude a_r, marked with squares in the plot. In addition, there are four pairs of

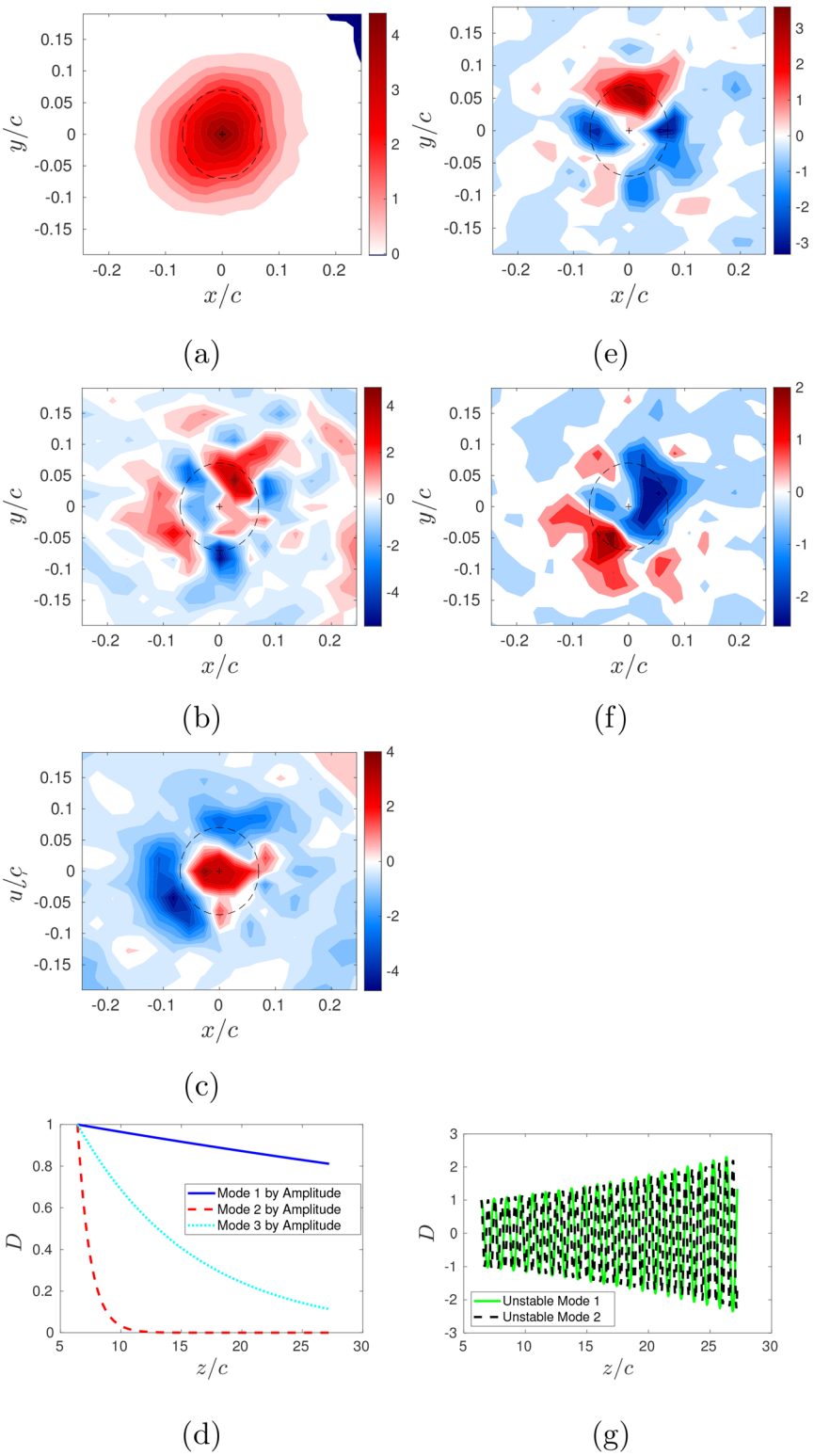

FIG. 10. Analysis over the intermediate field: (a)–(c) real part of the leading HODMD modes $\boldsymbol{q}$ in terms of amplitude, (d) the associated temporal dynamics, (e) and (f) real part of the leading HODMD modes $\boldsymbol{q}$ in terms of decreasing amplification factor δ_n and (g) the associated dynamics.

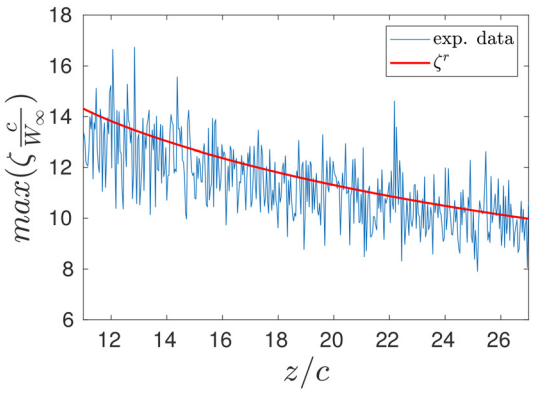

FIG. 11. Comparison of experimental maximum vorticity and the one reconstructed using modes 1, 2, and 3 following Eq. (18).

conjugates (unstable modes) with $\delta_r > 0$. The two modes with the highest δ_r have been marked with stars.

The structure of the three real modes is shown in Figs. 10(a)–10(c) in order of decreasing amplitude, together with the dynamics in Fig. 10(d). Mode 1 is similar to the mean flow and has a slow decay. Mode 2 has some smaller structures and it is associated with a transient decay with a very small value at about 1/3 of the spatial domain. Mode 3 appears to be a mode with an annular structure with some loss of axisymmetric (c) and with stronger decay than mode 1. Note that modes 1 and 3 in the intermediate field have a similar structure to modes 1 and 2 in the whole domain, compare Figs. 10(a) and 10(c) with Figs. 6(a) and 6(b). This fact is reasonable since the intermediate region is about 3 times larger than the near or far field regions, and therefore, it has a stronger influence on the computation of the whole field using HODMD. Figures 10(e) and 10(f) show the two most unstable modes together with their downstream dynamics in Fig. 10(g). Both of them have dipole-like structure as the rest of the unstable modes in this region (not shown).

It is interesting to analyze how the decay of modes 1, 2, and 3 can be directly related to the decay of the maximum of the vorticity. To that end, we reconstruct the maximum of the dimensionless vorticity in each plane using the expression

$$\max\zeta^r(z) = a_1 \max(\hat{\boldsymbol{q}}_1)D_1(z) + a_2 \max(\hat{\boldsymbol{q}}_2)D_2(z) + a_3 \max(\hat{\boldsymbol{q}}_1)D_3(z). \quad (17)$$

Since these three modes have real spectral values, (17) is equivalent to

$$\max\zeta^r(z) = \sum_{j=1}^{3} a_j \max(\hat{\boldsymbol{q}}_j) e^{\delta_j z/W_\infty}. \quad (18)$$

Figure 11 shows the experimental data together with the reconstruction using only three modes in the intermediate field. Neglecting a transient within approximately $3.5c$ after the beginning of the intermediate field, it is observed that the agreement is quite good to capture the mean decay. Fitting both data to linear approximations provides a mean slope of –0.2232 in the raw experimental data and −0.2563 in the approximation. This ability of HODMD of capturing the decay is very relevant applications focusing on vortex alleviation. Furthermore, the decay is obtained only from a few leading DMD modes, giving a reduced-order model consistent with the use of HODMD, which consists of a useful tool for low space but high time complex data.[19]

c. Far field. We applied HODMD to the far field, defined as $z/c > 27.25$, obtaining 12 unique physically relevant modes.

The amplitude, frequency, and decay associated with these modes are shown in Fig. 12. The leading modes in terms of amplitude and the two most unstable modes are marked with squares and stars, respectively. Similar to what happens in the near field, there is only one real mode. In addition, there are four pairs of unstable modes some of them with very high amplitude. Note also that in this region the most unstable modes have a δ_r much bigger than in the other regions leading to a higher amplification.

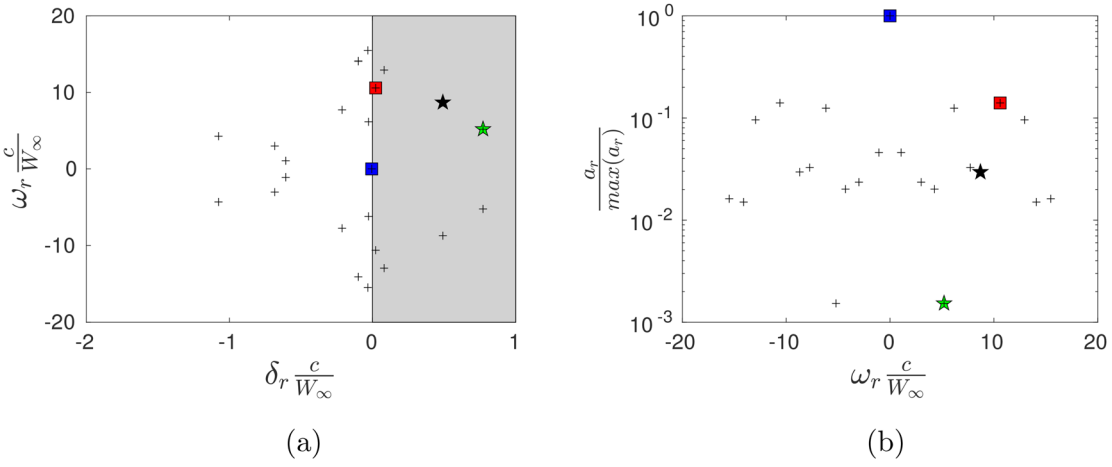

FIG. 12. HODMD analysis to the far field: (a) amplification factor vs frequency and (b) frequencies vs amplitude. In both pictures, the modes with highest amplitude are marked with squares: mode 1 in blue and mode 2 in red. The most unstable modes are marked with colored stars: mode 1 in green and mode 2 in black.

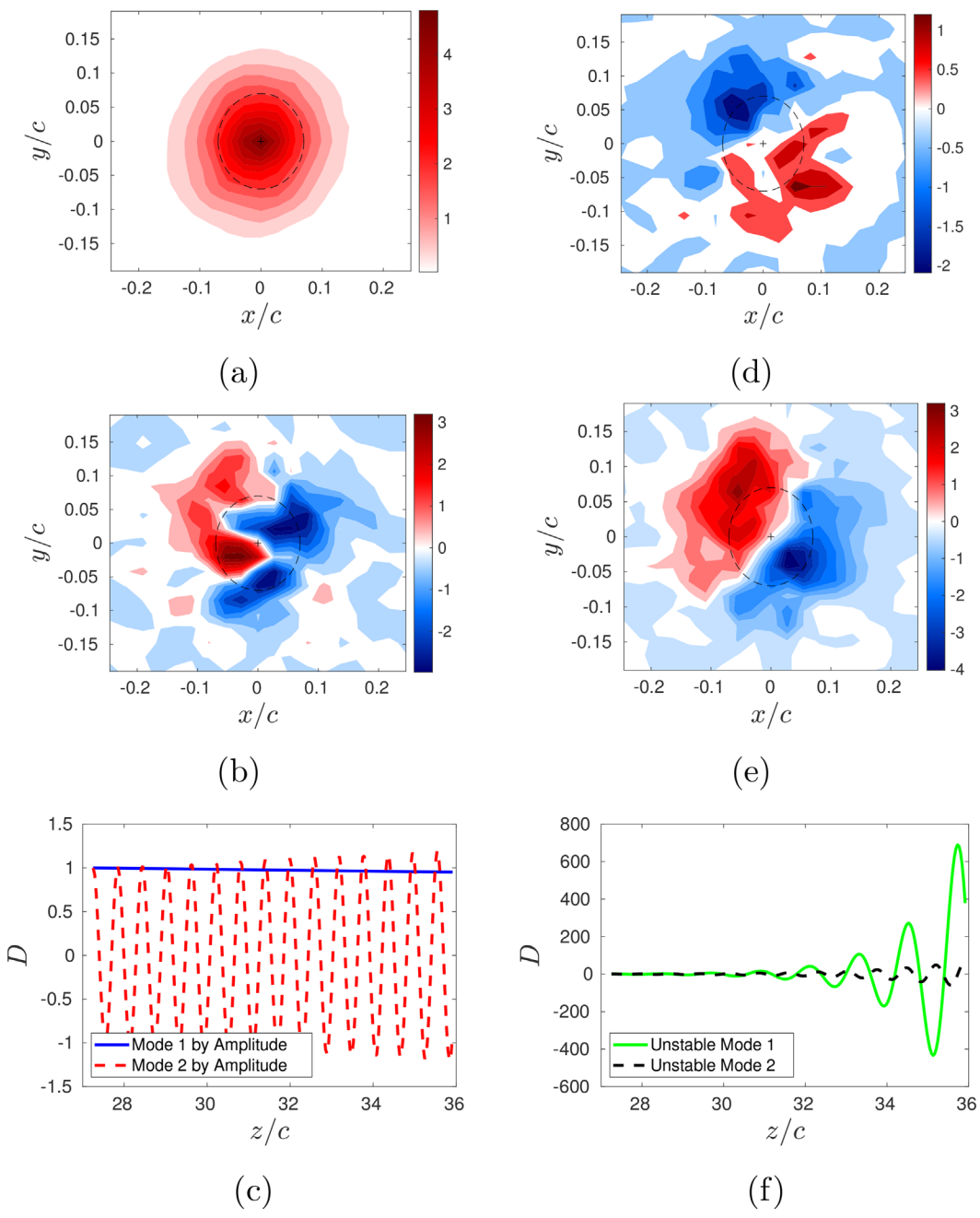

FIG. 13. Analysis over the far field: (a) and (b) real part of the leading HODMD modes $\boldsymbol{q}$ in terms of amplitude, (c) the associated temporal dynamics, (d) and (e) real part of the leading HODMD modes $\boldsymbol{q}$ in terms of decreasing amplification factor δ_r, and (f) the associated dynamics.

The spatial structure of the first two modes in order of amplitude are shown in Figs. 13(a) and 13(b) along with their downstream dynamic (c). Again, the first mode is real, and it is associated with the mean flow and has almost no decay. The second strongest mode in amplitude is already an unstable mode, and it is associated with a dipole-like structure. In this particular case, the shape of the dipole with a spiral concentration near the vortex core has to be noted. Figures 13(d) and 13(e) display the two modes with the highest δ_r together with their downstream dynamic in (f). The downstream dynamics of the mode with the highest δ_r shows a huge amplification in only a few chords. To sum up, in the far field it was possible to find unstable modes with both the highest amplitude a_r and the highest δ_r.

V. CONCLUSION

We have applied HODMD to (noisy) experimental data obtained by stereoscopic (2D3C-)PIV in the turbulent wake of a wing model with a NACA0012 airfoil. In particular, HODMD has been applied to the vorticity field. HODMD demonstrated a great ability to extract temporal information neglecting the experimental noise.

The results of the HODMD technique are relevant in three fundamental aspects. First, despite the experimental noise, HODMD can be successfully applied either to the whole spatial domain or to different areas of it. In particular, it was found that partitioning by zones along the z axis yields a better identification of the most important modes for the reduction of the trailing vortex model. Second, the modes with larger amplitude a_r are real and are associated with the vortex decay in the base flow. Third, there are unstable modes, with $\delta_r > 0$, in all the regions but the near region where all modes are stable. The unstable modes have always been identified with a dipole structure. To the best of our knowledge, this is the first study on instabilities in a streamwise oriented wake vortex in non-turbulent initial conditions.

The motivation of this paper was to identify the dynamic modes governing vortex decay within 36 chords behind the wing, which permit to derive reduced-order models of the trailing vortex dynamics. Such models are of highest importance for the design of efficient control strategies. Our HODMD analysis shows that, in this downstream range, the trailing vortex is decaying while being subject to amplified oscillations beyond about six chords behind the wing (that is, in the intermediate and far field). With this information, it will be feasible to introduce active control in an experiment, thus forcing the vortex decay more efficiently.

ACKNOWLEDGMENTS

This work was supported in part by the Ministerio de Ciencia e Innovación of Spain (Grant No. PID2021–124692OA-I00). This work was supported in part by the project B4-2019-11, 0837002010 from the Universidad de Málaga. Funding for open access charge: Universidad de Málaga.

AUTHOR DECLARATIONS

Conflict of Interest

The authors have no conflicts to disclose.

Author Contributions

P. Gutierrez Castillo: Conceptualization (equal); Investigation (equal); Methodology (equal); Supervision (equal); Validation (equal); Writing – original draft (equal); Writing – review & editing (equal). **M. Garrido-Martin:** Investigation (equal); Methodology (equal); Validation (equal); Writing – original draft (equal); Writing – review & editing (equal). **T. Bölle:** Investigation (equal); Methodology (equal); Validation (equal); Writing – original draft (equal); Writing – review & editing (equal). **J. H. García-Ortiz:** Data curation (equal); Investigation (equal); Visualization (equal); Writing – review & editing (equal). **J. Aguilar-Cabello:** Data curation (equal); Visualization (equal); Writing – review & editing (equal). **C. del Pino:** Conceptualization (equal); Investigation (equal); Supervision (equal); Validation (equal); Writing – original draft (equal); Writing – review & editing (equal).

DATA AVAILABILITY

The data that support the findings of this study are available from the corresponding author upon reasonable request.

APPENDIX A: ROBUSTNESS OF THE SOLUTION

In this appendix, we provide details about the robustness of the solutions upon parameter variations.

First of all, we discuss the time resolution. Previous experiments provide considerable evidence that the governing vortex dynamics is of low frequency. For instance, vortex meandering is typically associated with frequencies of the order of $\omega \frac{c}{W_\infty} \sim 1$. This is about two orders of magnitude slower than our sampling rate $\omega_s \frac{c}{W_\infty} = 2\pi f_2 \frac{c}{W_\infty} \sim 180$.

Nevertheless, and in order to verify the temporal resolution of the experiment for the dynamics of interest using HODMD, we introduced a skipping parameter $r \geq 1$ to select only every rth image from the recording. Hence, we obtain the reduced snapshot matrix $\Phi_r := [\phi(1), \phi(1+r), \phi(1+2r), \ldots]$, where $\phi(k) \in \mathbb{R}^M$ denotes the spatial data of the kth measurement (M measurement points in the plane). In particular, we have analyzed the whole time series ($r = 1$) and repeated the analysis with only half of the snapshots (using every other snapshot, i.e., $r = 2$). The results show that the error found in both cases is equivalent and also that the optimal d value for both cases is comparable in the used range of snapshots (one has twice the value of the second one). The proof about the value of d when reducing the number of snapshots is given in the State of Art.[20]

Second, we discuss the domain size. The original domain was recentered in the position of the maximum vorticity considering the center point and nine grid points to each side. Thus, yielding a 19×19 grid with $\delta x = 0.272$ and $\delta y = 0.211$ cm. Therefore, the computational domain extends over approximately three core radii. However, HODMD has shown to be robust in terms of the size of the domain. To prove that, HODMD was computed from 15×15 to 23×23 grid points without any significant change in the results.

Third, we discuss the threshold of ϵ_{DMD}. ϵ_{DMD} that was selected relatively small in order to capture the unstable modes since these modes could be associated with small scale fluctuations. Note that there are mean modes with higher order amplitude in general. Nevertheless, we have found some instabilities of high amplitude making the conclusion of having unstable modes robust to any reasonable variation of ϵ_{DMD}.

Last, we discuss the influence of the position of the divisions of the different regions of the z domain. The divisions to define the different z domains were computed minimizing the error with linear interpolation as described on Sec. IV. However, we have varied the limits of the different domains in a reasonable range finding similar spatial modes with frequencies associated within a small error margin of less than 10%, similar to other recent HODMD studies.[38]

APPENDIX B: MODES DATA

This appendix, in Tables II–V includes the data of the unique physically relevant modes in each of the z regions to complement the figures presented in the paper. Note that the tables include only $\omega_r > 0$ values but all the complex modes come in pairs of complex conjugates

TABLE II. Whole field.

Mode no.	Amplitude $\frac{a_r}{\max(a_r)}$	Damping factor $\delta_r \frac{c}{W_\infty}$	Frequency $\omega_r \frac{c}{W_\infty}$	Mode no.	Amplitude $\frac{a_r}{\max(a_r)}$	Damping factor $\delta_r \frac{c}{W_\infty}$	Frequency $\omega_r \frac{c}{W_\infty}$
1	1.0000	−0.0012	0.0000	41	0.0167	−0.2036	2.9054
2	0.7729	−0.1318	0.0000	42	0.0164	−0.1027	11.1938
3	0.2655	−0.3621	1.2574	43	0.0160	−0.1896	14.5854
4	0.2262	−0.2793	0.6429	44	0.0153	−0.3372	3.4258
5	0.1910	−0.0718	0.1698	45	0.0152	−0.1338	12.0740
6	0.0910	−0.1063	1.1086	46	0.0144	−0.0325	9.9786
7	0.0788	−0.5046	12.6464	47	0.0140	−0.0782	9.1654
8	0.0682	−0.3098	6.0388	48	0.0134	−0.0454	5.4513
9	0.0660	−0.2162	10.0544	49	0.0131	−0.0119	4.4463
10	0.0607	−0.3168	6.4251	50	0.0122	−0.0386	2.0763
11	0.0565	−0.1477	15.6568	51	0.0116	−0.1742	8.8894
12	0.0550	−0.2785	15.8858	52	0.0113	**0.0035**	10.9985
13	0.0531	−0.1589	2.2990	53	0.0112	−0.0501	8.2744
14	0.0513	−0.0773	1.4170	54	0.0111	−0.0608	12.4417
15	0.0466	−0.1613	7.7168	55	0.0100	−0.0479	7.9954
16	0.0461	−0.3392	13.1328	56	0.0097	**0.0133**	15.2346
17	0.0371	−0.1012	0.8748	57	0.0090	**0.0120**	14.8375
18	0.0367	−0.1346	15.4829	58	0.0088	−0.1051	16.1846
19	0.0363	−0.1632	12.8592	59	0.0084	−0.1208	3.6261
20	0.0352	−0.2311	8.6181	60	0.0079	−0.0443	1.6365
21	0.0338	−0.1767	7.0670	61	0.0077	−0.0201	10.4633
22	0.0313	−0.1119	11.4251	62	0.0075	−0.0117	11.9673
23	0.0305	−0.1268	8.4721	63	0.0068	−0.0604	3.1034
24	0.0301	−0.0771	3.9969	64	0.0068	**0.0244**	7.3802
25	0.0288	−0.1020	13.8469	65	0.0062	−0.1201	6.7902
26	0.0285	−0.0922	2.6112	66	0.0057	−0.0324	4.9610
27	0.0271	−0.0309	10.1563	67	0.0056	**0.0304**	7.1668
28	0.0248	−0.0331	0.5531	68	0.0052	**0.0089**	3.2339
29	0.0248	−0.1759	16.3536	69	0.0050	**0.0384**	2.5759
30	0.0244	−0.2457	14.0315	70	0.0049	−0.0713	5.7591
31	0.0238	−0.0551	4.6691	71	0.0047	**0.0105**	6.5509
32	0.0238	−0.1527	9.5319	72	0.0043	−0.0821	5.0679
33	0.0226	−0.0488	5.2983	73	0.0042	**0.0350**	3.8663
34	0.0219	−0.2274	10.6359	74	0.0034	**0.0454**	6.2059
35	0.0198	−0.0533	9.6383	75	0.0032	**0.0121**	14.5047
36	0.0192	−0.0904	13.4258	76	0.0025	−0.0714	1.8938
37	0.0191	−0.1361	4.3234	77	0.0019	**0.0709**	7.6851
38	0.0191	−0.1028	14.2592	78	0.0018	**0.0718**	11.6100
39	0.0181	−0.0487	8.9788	79	0.0014	**0.0895**	13.0386
40	0.0179	−0.0618	6.0465	80	0.0011	**0.0991**	10.8601

TABLE III. Near field.

Mode no.	Amplitude $\frac{a_r}{\max(a_r)}$	Damping factor $\delta_r \frac{c}{W_\infty}$	Frequency $\omega_r \frac{c}{W_\infty}$
1	1	−0.0015	0.0000
2	0.0429	−0.9680	6.1911
3	0.0336	−0.6981	12.2144
4	0.0259	−0.8766	14.8737
5	0.0205	−0.8152	3.3381
6	0.007	−1.1782	8.9696

so the same mode with negative frequency exists and is associated with the same spatial mode. The modes are sorted in order of amplitude and the unstable modes are marked with bold letters.

TABLE V. Far field.

Mode no.	Amplitude $\frac{a_r}{\max(a_r)}$	Damping factor $\delta_r \frac{c}{W_\infty}$	Frequency $\omega_r \frac{c}{W_\infty}$
1	1.0000	−0.0058	0.0000
2	0.1405	**0.0219**	10.6036
3	0.1248	−0.0281	6.1717
4	0.0959	**0.0808**	12.9505
5	0.0458	−0.6065	1.0679
6	0.0326	−0.2128	7.7308
7	0.0295	**0.4912**	8.7049
8	0.0236	−0.6831	2.9952
9	0.0202	−1.0762	4.2854
10	0.0162	−0.0329	15.4810
11	0.0151	−0.0992	14.0935
12	0.0015	**0.7720**	5.2025

TABLE IV Intermediate field.

Mode no.	Amplitude $\frac{a_r}{\max(a_r)}$	Damping factor $\delta_r \frac{c}{W_\infty}$	Frequency $\omega_r \frac{c}{W_\infty}$	Mode no.	Amplitude $\frac{a_r}{\max(a_r)}$	Damping factor $\delta_r \frac{c}{W_\infty}$	Frequency $\omega_r \frac{c}{W_\infty}$
1	1.0000	−0.0101	0.0000	24	0.0163	−0.1136	0.5672
2	0.6082	−0.9523	0.0000	25	0.0160	−0.1210	16.7830
3	0.3679	−0.1046	0.0000	26	0.0152	−0.0106	15.6430
4	0.0976	−0.4940	5.1412	27	0.0149	−0.0689	14.6285
5	0.0525	−0.1423	9.7615	28	0.0145	−0.1721	1.8594
6	0.0408	−0.1788	8.9078	29	0.0144	−0.0810	11.6622
7	0.0362	−0.1121	1.0956	30	0.0140	−0.0300	10.2655
8	0.0326	−0.1035	9.8954	31	0.0139	−0.0587	14.1894
9	0.0315	−0.2737	5.6492	32	0.0134	−0.1734	15.9467
10	0.0309	−0.3688	3.2078	33	0.0117	−0.0517	15.1788
11	0.0297	−1.1527	10.9055	34	0.0114	**0.0072**	3.3120
12	0.0281	−0.0332	1.4511	35	0.0110	−0.0012	6.4754
13	0.0258	−0.0963	16.4237	36	0.0109	−0.0079	10.8594
14	0.0256	−0.0868	3.9049	37	0.0106	**0.0033**	9.1846
15	0.0255	−0.3856	8.3214	38	0.0092	−0.0810	12.0172
16	0.0241	−0.0440	13.7771	39	0.0089	−0.1288	12.8696
17	0.0223	−0.1956	4.3039	40	0.0077	−0.0250	8.2263
18	0.0222	−0.0771	2.3560	41	0.0072	**0.0420**	5.9963
19	0.0213	−0.1352	2.8025	42	0.0071	−0.0629	12.4596
20	0.0211	−0.1021	4.7648	43	0.0068	**0.0393**	11.3708
21	0.0210	−0.0943	13.4202	44	0.0018	−0.0875	6.9158
22	0.0182	−0.0633	7.8579	45	0.0017	−0.1571	5.2008
23	0.0175	−0.0401	7.3852				

REFERENCES

[1]F. Castro, A. Crespo, F. Manuel, and D. H. Fruman, "Equilibrium of ventilated cavities in tip vortices," J. Fluids Eng. **119**, 759–767 (1997).
[2]M. Felli and M. Falchi, "Propeller tip and hub vortex dynamics in the interaction with a rudder," Exp. Fluids **51**, 1385–1402 (2011).
[3]P. Spalart, "Airplane trailing vortices," Annu. Rev. Fluid Mech. **30**, 107–138 (1998).
[4]L. Jacquin and C. Pantano, "On the persistence of trailing vortices," J. Fluid Mech. **471**, 159–168 (2002).
[5]P. Panagiotou, G. Ioannidis, I. Tzivinikos, and K. Yakinthos, "Experimental investigation of the wake and the wingtip vortices of a UAV model," Aerospace **4**, 53 (2017).

[6]Z. Yu, Y. Qu, and Y. Zhang, "Safe control of trailing UAV in close formation flight against actuator fault and wake vortex effect," Aerosp. Sci. Technol. **77**, 189–205 (2018).
[7]J. N. Hallock and F. Holzäpfel, "A review of recent wake vortex research for increasing airport capacity," Prog. Aerosp. Sci. **98**, 27–36 (2018).
[8]J. Van Jaarsveld, A. Holten, A. Elsenaar, R. Trieling, and G. van Heijst, "An experimental study of the effect of external turbulence on the decay of a single vortex and a vortex pair," J. Fluid Mech. **670**, 214–239 (2011).
[9]J. H. García-Ortiz, F. J. Blanco-Rodríguez, L. Parras, and C. del Pino, "Experimental observations of the effects of spanwise blowing on the wingtip vortex evolution at low Reynolds numbers," Eur. J. Mech.-B/Fluids **80**, 133–145 (2020).
[10]F. Blanco-Rodríguez, L. Parras, and C. del Pino, "Frequency response of Lamb-Oseen vortex," Fluid Dyn. Res. **48**, 061417 (2016).
[11]J. Kostas, J. Soria, and M. S. Chong, "A comparison between snapshot POD analysis of PIV velocity and vorticity data," Exp. Fluids **38**, 146–160 (2005).
[12]G. Berkooz, P. Holmes, and J. L. Lumley, "The proper orthogonal decomposition in the analysis of turbulent flows," Annu. Rev. Fluid Mech. **25**, 539–575 (1993).
[13]P. Holmes, J. L. Lumley, and G. Berkooz, *Turbulence, Coherent Structures, Dynamical Systems and Symmetry* (Cambridge University Press, 1996).
[14]C. del Pino, J. López-Alonso, L. Parras, and R. Fernandez-Feria, "Dynamics of the wing-tip vortex in the near field of a NACA 0012 aerofoil," Aeronaut. J. **115**, 229–239 (2011).
[15]M. Dghim, M. Ferchichi, and H. Fellouah, "On the effect of active flow control on the meandering of a wing-tip vortex," J. Fluid Mech. **896**, A30 (2020).
[16]T. Bölle, V. Brion, J.-C. Robinet, D. Sipp, and L. Jacquin, "On the linear receptivity of trailing vortices," J. Fluid Mech. **908**, A8 (2021).
[17]C. W. Rowley, I. Mezić, S. Bagheri, P. Schlatter, and D. S. Henningson, "Spectral analysis of nonlinear flows," J. Fluid Mech. **641**, 115–127 (2009).
[18]P. J. Schmid, "Dynamic mode decomposition of numerical and experimental data," J. Fluid Mech. **656**, 5–28 (2010).
[19]P. J. Schmid, "Dynamic mode decomposition and its variants," Annu. Rev. Fluid Mech. **54**, 225–254 (2022).
[20]S. Le Clainche and J. M. Vega, "Higher order dynamic mode decomposition," SIAM J. Appl. Dyn. Syst. **16**, 882–925 (2017).
[21]J. M. Vega and S. Le Clainche, *Higher Order Dynamic Mode Decomposition and Its Applications* (Elsevier, 2021).
[22]S. Le Clainche and J. M. Vega, "Higher order dynamic mode decomposition to identify and extrapolate flow patterns," Phys. Fluids **29**, 084102 (2017).
[23]S. Le Clainche, J. Kuo, and W. Zhang, "A reduced-order model for compressible flows with buffeting condition using higher order dynamic mode decomposition with a mode selection criterion," Phys. Fluids **30**, 016103 (2018).
[24]S. Le Clainche, J. M. Vega, and J. Soria, "Higher order dynamic mode decomposition of noisy experimental data: The flow structure of a zero-net-mass-flux jet," Exp. Therm. Fluid Sci. **88**, 336–353 (2017).
[25]S. Le Clainche, D. Rodríguez, V. Theofilis, and J. Soria, "Flow around a hemisphere-cylinder at high angle of attack and low Reynolds number. Part II: POD and DMD applied to reduced domains," Aerosp. Sci. Technol. **44**, 88–100 (2015).
[26]L. Zhou, K. Tse, G. Hu, and Y. Li, "Higher order dynamic mode decomposition of wind pressures on square buildings," J. Wind Eng. Ind. Aerodyn. **211**, 104545 (2021).
[27]J. H. García-Ortiz, A. Domínguez-Vázquez, J. Serrano-Aguilera, L. Parras, and C. del Pino, "A complementary numerical and experimental study of the influence of Reynolds number on theoretical models for wingtip vortices," Comput. Fluids **180**, 176–189 (2019).
[28]L. Graftieaux, M. Michard, and N. Grosjean, "Combining PIV, POD and vortex identification algorithms for the study of unsteady turbulent swirling flows," Meas. Sci. Technol. **12**, 1422–1429 (2001).
[29]G. V. Iungo, P. Skinner, and G. Buresti, "Correction of wandering smoothing effects on static measurements of a wing-tip vortex," Exp. Fluids **46**, 435–452 (2009).
[30]G. V. Iungo, "Wandering of a wing-tip vortex: Rapid scanning and correction of fixed-point measurements," J. Aircr. **54**, 1779–1790 (2017).
[31]P. Meunier and T. Leweke, "Analysis and treatment of errors due to high velocity gradients in particle image velocimetry," Exp. Fluids **35**, 408–421 (2003).
[32]M. Kamb, E. Kaiser, S. L. Brunton, and J. N. Kutz, "Time-delay observables for Koopman: Theory and applications," SIAM J. Appl. Dyn. Syst. **19**, 886–917 (2020).
[33]L. Sirovich, "Turbulence and the dynamics of coherent structures. I. Coherent structures," Q. Appl. Math. **45**, 561–571 (1987).
[34]F. Riesz and B. Sz-Nagy, *Functional Analysis* (Dover Publications, Inc., New York, 1955).
[35]H. J. Tu, C. W. Rowley, and D. M. Luchtenburg, "On dynamic mode decomposition: Theory and applications," J. Comput. Dyn. **1**, 391–421 (2014).
[36]H. C. Ghimire and S. C. C. Bailey, "An experimental investigation of wing-tip vortex decay in turbulence," Phys. Fluids **29**, 037108 (2017).
[37]C. Cerreteli and C. H. K. Williamson, "The physical mechanism for vortex merging," J. Fluid Mech. **475**, 41–77 (2003).
[38]S. Le Clainche, M. E. Rosti, and L. Brandt, "A data-driven model based on modal decomposition: Application to the turbulent channel flow over an anisotropic porous wall," J. Fluid Mech. **939**, A5 (2022).